

## Seyfert Galaxies as Neutrino Sources: An Outflow–Cloud Interaction Perspective

ZHI-PENG MA ,<sup>1</sup> KAI WANG ,<sup>1</sup> YUAN-YUAN ZUO ,<sup>1</sup> YUAN-CHUAN ZOU ,<sup>1</sup> AND YONG-HAN HUANG<sup>1</sup>

<sup>1</sup>Department of Astronomy, School of Physics, Huazhong University of Science and Technology, Wuhan, Hubei 430074, China

### ABSTRACT

Following the identification of the first confirmed individual neutrino source, Seyfert galaxies have emerged as the most prominent class of high-energy neutrino emitters. In this work, we perform a detailed investigation of the outflow–cloud interaction scenario for neutrino production in Seyfert nuclei. In this framework, fast AGN-driven winds collide with clumpy gas clouds in the nuclear region, forming bow shocks that efficiently accelerate cosmic-ray protons. The accelerated protons subsequently interact with cold protons from the outflows via inelastic proton–proton ( $pp$ ) collisions, producing high-energy neutrinos, while the photomeson ( $p\gamma$ ) process with disk photons may provide a subdominant contribution at the highest energies. Applying this model to five neutrino-associated Seyfert galaxies, we successfully reproduce the observed TeV neutrino fluxes without violating existing gamma-ray constraints. By integrating over the Seyfert population using X-ray luminosity functions, we further demonstrate that Seyfert galaxies can account for a substantial fraction of the diffuse astrophysical neutrino background in the  $10^4$ – $10^5$  GeV energy range.

*Keywords:* Neutrino astronomy — High energy astrophysics — Active galactic nuclei

### 1. INTRODUCTION

High-energy neutrinos provide a unique probe of non-thermal processes in the universe. Since the first detection of a diffuse neutrino flux in the  $10$ – $10^3$  TeV range by the IceCube Collaboration in 2013 (I. Collaboration\* 2013), the sources responsible for these fluxes have remained largely unidentified. In 2022, however, the IceCube Collaboration reported compelling evidence for the emission of  $1$ – $10$  TeV neutrinos from the Seyfert II galaxy NGC 1068 at a significance level of  $4.2\sigma$  (R. Abbasi et al. 2022). A subsequent analysis further increased the significance to  $5.0\sigma$ , establishing NGC 1068 as a firmly confirmed neutrino source (R. Abbasi et al. 2025). In addition to NGC 1068, the recently identified NGC 7469 shows the second strongest signal, with a significance of  $3.8\sigma$  (R. Abbasi et al. 2025); this galaxy had previously been proposed to coincide spatially with two  $\sim 100$  TeV neutrino events (G. Sommani et al. 2025). Furthermore, follow-up IceCube searches for neutrino emission from X-ray–bright AGN have revealed suggestive excesses (at  $\lesssim 3\sigma$  significance) from several other Seyfert galaxies, including NGC 4151, NGC 3079, and CGCG 420–015 (R. Abbasi et al. 2025; A. Neronov et al.

2024). These findings indicate that Seyfert galaxies currently represent the most prominent class of high-energy neutrino emitters.

Several theoretical scenarios have been proposed to explain the origin of neutrinos and gamma rays from Seyfert nuclei. Protons may be stochastically accelerated in the coronal plasma and subsequently interact with X-ray coronal photons to produce neutrinos (K. Murase et al. 2020; A. Kheirandish et al. 2021; M. Lemoine & F. Rieger 2025). Proton acceleration via magnetic reconnection has also been investigated (R. Mbarek et al. 2024; D. F. Fiorillo et al. 2024, 2025), as well as through accretion shock mechanisms (K. Murase et al. 2024). On larger spatial scales, neutrino and gamma-ray production resulting from jet–interstellar medium (ISM) interactions has been studied (K. Fang et al. 2023). A two-zone model has also been developed that incorporates both the corona and starburst regions to account for the observed gamma-ray emissions (B. Eichmann et al. 2022). Meanwhile, supernova explosions or compact binary mergers occurring within the accretion disks of AGNs have been proposed as additional potential sources of high-energy neutrinos (J.-P. Zhu et al. 2021; Z.-P. Ma & K. Wang 2024; Z.-H. Zhou et al. 2023; Z.-H. Zhou & K. Wang 2023). Even for jetted AGNs, such as the well-known neutrino candidate TXS 0506+056, similar production mechanisms

Corresponding author: Kai Wang  
 kaiwang@hust.edu.cn

have been considered (I. Collaboration et al. 2018; D. F. Fiorillo et al. 2025).

In addition to the aforementioned models, AGNs can also drive outflows with velocities ranging from  $300 \text{ km s}^{-1}$  to  $0.3c$ , which are believed to be launched from the accretion disk via radiative or magnetohydrodynamic (MHD) mechanisms (S. Laha et al. 2021; C. Harrison et al. 2018). Such outflows can generate shocks in the vicinity of the AGN, where particles may be accelerated by diffusive shock acceleration (DSA) (R. Blandford & D. Eichler 1987; A. Bell 2013; M. Malkov & L. O. Drury 2001). Several studies have invoked outflows to explain the neutrino emission observed from NGC 1068 (S. Inoue et al. 2022; A. Lamastra et al. 2016). In our previous study, we proposed that AGN-driven outflows may interact with dark clouds embedded in the coronal region (Y.-H. Huang et al. 2024). The bow shocks generated by the outflow–cloud interactions can accelerate protons, which then undergo hadronic interactions with the ambient gas or radiation fields, producing high-energy neutrinos. This mechanism can potentially account for the neutrino emission observed from NGC 1068. In this work, we present a more detailed analysis of the outflow–cloud interaction model for Seyfert nuclei. We investigate the dominant hadronic processes and emphasize the parameter dependencies within this framework. We then extend our study to all known neutrino-associated Seyfert galaxies to reproduce their observed neutrino and gamma-ray fluxes. Finally, we explore the contributions of the entire Seyfert galaxy population to the diffuse neutrino and gamma-ray backgrounds.

The structure of this paper is as follows. In Section 2, we review the physical framework of the outflow–cloud interaction model and describe the hadronic processes involved. In Section 3, we apply the model to individual Seyfert galaxies, using NGC 1068 as a case study to illustrate parameter dependencies. We also evaluate the contributions to the diffuse neutrino and gamma-ray backgrounds from the overall Seyfert population. Finally, we summarize our findings in Section 4.

## 2. MODEL REVIEW

### 2.1. *Dynamic Process*

As discussed in previous studies of NGC 1068, the observed neutrino emission from Seyfert galaxies is likely produced in the AGN corona region (Y. Inoue et al. 2020; L. A. Anchordoqui et al. 2021; K. Murase 2022; P. Padovani et al. 2024b; A. Kheirandish et al. 2021). In our scenario, we assume the presence of long-lived, clumpy gas that is distributed quasi-isotropically and uniformly around the supermassive black hole (SMBH)

within the corona region. These clumps (hereafter referred to as *clouds*) may originate from supernova explosions in the inner region of the star-forming disk and are subsequently driven outward along magnetic field lines by the disk radiation pressure, eventually forming a metal-rich broad-line region (BLR) (J.-M. Wang et al. 2012; B. Czerny & K. Hryniewicz 2011; M.-H. Naddaf & B. Czerny 2024). The clouds are assumed to be long-lived, as continuous mass circulation between the star-forming disk and the BLR can sustain the gas supply. The geometric size and number density of such clouds are set to  $r_c \simeq 10^9 \text{ cm}$  and  $n_c \simeq 5 \times 10^{22} \text{ cm}^{-3}$ , based on the typical density of the outer part of red giant star (J.-C. Passy et al. 2012). The cloud location is parameterized as  $r_0 = \mathcal{R}R_s$ , where  $R_s = 2GM_\bullet/c^2$  is the Schwarzschild radius and  $M_\bullet$  is the mass of SMBH. In our model,  $r_0$  is treated as a free parameter, while it must be larger than the tidal disruption radius  $r_d$ , i.e.,  $r_0 > r_d \simeq 13R_{s,12.5} M_{\bullet,7}^{-2/3} n_{c,22.7}^{-1/3}$ , to avoid the SMBH disrupting the clouds (E. M. Rossi et al. 2021). The conventional notation  $Q_x = Q/10^x$  in cgs units is adopted hereafter.

In Seyfert galaxies, the typical outflow velocity is in the range of  $v_0 \simeq 0.03\text{--}0.3c$  (E. Peretti et al. 2023; M. Mizumoto et al. 2019). The associated kinetic luminosity is often parameterized as a fraction of the AGN bolometric luminosity, i.e.,  $L_{\text{kin}} = \eta_k L_{\text{bol}}$ , where  $\eta_k \leq 1$ . In principle, such outflows can manifest as blue-shifted atomic absorption features in the ultraviolet (UV) to X-ray bands (S. Veilleux et al. 2005; A. King & K. Pounds 2015; S. Laha et al. 2021). However, direct observations of outflows in Seyfert galaxies are challenging, largely due to obscuration by the thick gas and dust (S. García-Burillo et al. 2016; V. Gámez Rosas et al. 2022; G. Matt et al. 1997). Nevertheless, there is observational evidence supporting their existence in some cases, such as the well-studied Seyfert galaxy NGC 4151 (E. Peretti et al. 2023). These high-speed, quasi-isotropic outflows may collide with the clouds at a distance  $r_0$  (H.-J. Wu et al. 2022; H. Wu et al. 2024), generating a bow shock outside the cloud and a cloud shock inside it, with characteristic velocities  $v_0$  and  $v_c$ , respectively (C. F. McKee & L. L. Cowie 1975). Both shocks are capable of accelerating protons. We can connect two shock velocities through the relation  $v_c \simeq (n_0/n_c)^{1/2}v_0$ , where  $n_0 \simeq 6.6 \times 10^{12} \eta_{k,-1} L_{\text{bol},45} (\mathcal{R}/15)^{-2} R_{s,12.5}^{-2} (v_0/0.03c)^{-3} \text{ cm}^{-3}$  is the outflow number density at  $r_0$  (C. F. McKee & L. L. Cowie 1975; G. Mou & W. Wang 2021). The density ratio  $n_0/n_c$  must be less than unity to prevent the outflows from destroying clouds, this yields  $t_{\text{bs}}/t_{\text{cs}} \approx (v_c/v_0)^2 = (n_0/n_c) < 1$ , where  $t_{\text{bs}}$  and  $t_{\text{cs}}$

are the acceleration timescale for two shocks respectively (L. O. Drury 1983). This relation indicates that the bow shock is the dominant acceleration site; thus, we only consider the neutrino and gamma-ray production from the bow shock. Particles are continuously accelerated until the cloud shock has swept through the entire cloud; the total duration of the acceleration process is thus set by (R. I. Klein et al. 1994)

$$t_{\text{cloud}} = \frac{r_c}{v_c} \simeq 9.7 \times 10^5 \eta_{k,-1}^{-1/2} r_{c,9} \left( \frac{\mathcal{R}}{15} \right) R_{s,12.5} r_{c,9} \times \left( \frac{n_{c,22.7}}{L_{\text{bol},45}} \right)^{1/2} \left( \frac{v_0}{0.03c} \right)^{1/2} \text{ s.} \quad (1)$$

## 2.2. Hadronic Processes

In this section, we analyze the timescales for particle acceleration and interaction to determine the dominant process responsible for neutrino production. The bow shock can efficiently accelerate protons to high energies via the DSA mechanism. The total proton luminosity is estimated as  $L_p \simeq \alpha\beta L_{\text{kin}} = 9 \times 10^{42} \eta_{k,-1} L_{\text{bol},45} \text{ erg s}^{-1}$ , where  $\alpha \sim 0.3$  is the cloud covering factor and  $\beta \sim 0.3$  is the energy fraction transferred to accelerated particles. The corresponding acceleration timescale is (L. O. Drury 1983)

$$t_{\text{acc}}^{-1} = \frac{3}{8} \frac{qBv_0^2}{E_p c} \simeq 0.06 \eta_{k,-1}^{1/2} L_{\text{bol},45}^{1/2} \epsilon_{B,-2}^{1/2} \left( \frac{\mathcal{R}}{15} \right)^{-1} R_{s,12.5}^{-1} \times \left( \frac{v_0}{0.03c} \right)^{3/2} \left( \frac{E_p}{50 \text{ TeV}} \right)^{-1} \text{ s}^{-1}, \quad (2)$$

where  $q$  is the proton charge,  $E_p$  is the proton energy, and  $\epsilon_B$  is the fraction of magnetic energy to the outflow kinetic energy, defined through  $B^2/8\pi = \epsilon_B \cdot L_{\text{kin}}/(4\pi r_0^2 v_0)$ .<sup>2</sup> The accelerated protons will have  $pp$  collisions with cold protons of the outflow, whose timescale is

$$t_{\text{pp}}^{-1} \approx 0.5 \sigma_{\text{pp}} n_0 c \simeq 3 \times 10^{-3} \eta_{k,-1} L_{\text{bol},45} \times \left( \frac{\mathcal{R}}{15} \right)^{-2} R_{s,12.5}^{-2} \left( \frac{v_0}{0.03c} \right)^{-3} \text{ s}^{-1}, \quad (3)$$

where  $pp$  cross section  $\sigma_{\text{pp}} \sim 5 \times 10^{-26} \text{ cm}^{-2}$  is adopted (D. Particle 2004). The accelerated protons can

<sup>2</sup> In many studies (e.g., K. Murase 2022; A. Das et al. 2024), the magnetic field is parameterized as  $\xi_B = U_B/U_\gamma$ , where  $U_\gamma = L_{\text{bol}}/(4\pi r_0^2 c)$  is the bolometric photon energy density. Note that  $\xi_B$  differs from  $\epsilon_B$  as defined in this work, but they are related by  $\xi_B \simeq 3.3 \times 10^{-2} \epsilon_{B,-2} \eta_{k,-1} (v_0/0.03c)^{-1}$ .

also undergo  $p\gamma$  interactions with soft photons originating from the corona and the disk. We model both photon fields following the approach proposed by K. Murase et al. (2020), in which the AGN bolometric luminosity  $L_{\text{bol}}$  can be estimated from the intrinsic X-ray luminosity  $L_X$  at 2-10 keV, using empirical correlations (P. F. Hopkins et al. 2007). The spectral energy distribution (SED) of AGN is parameterized as a function of the Eddington ratio (L. C. Ho 2008), defined as  $\lambda_{\text{Edd}} = L_{\text{bol}}/L_{\text{Edd}}$ , where the Eddington luminosity is given by  $L_{\text{Edd}} \approx 1.3 \times 10^{45} M_{\bullet,7} \text{ erg s}^{-1}$ . Using this method, the SED is fully determined by SMBH mass  $M_\bullet$  and the intrinsic X-ray luminosity  $L_X$ . See more details in Appendix B. The disk spectrum has the form of multi-color blackbody (N. I. Shakura & R. A. Sunyaev 1973), while the X-ray spectrum follows a power-law with an exponential cutoff (B. Trakhtenbrot et al. 2017a; C. Ricci et al. 2018), i.e.  $dn_X/d\epsilon_X \propto n_X^{-\Gamma_X} \exp(-\epsilon_X/\epsilon_{X,\text{cut}})$ . Based on this form of X-ray spectrum, the  $p\gamma$  interaction timescale between protons and X-ray photons is (K. Murase et al. 2008, 2016)

$$t_{p\gamma,X}^{-1} \simeq \eta_{p\gamma} \sigma_{p\gamma} \frac{L_X}{4\pi r_0^2 \epsilon_X} \left( \frac{E_p}{\tilde{E}_{p-X}} \right)^{\Gamma_X-1} \stackrel{\Gamma_X \approx 2}{\simeq} 2.1 \times 10^{-5} L_{X,43.7} \left( \frac{\mathcal{R}}{15} \right)^{-2} \times R_{s,12.5}^{-2} \left( \frac{E_p}{50 \text{ TeV}} \right) \text{ s}^{-1}, \quad (4)$$

where  $\eta_{p\gamma} = 2/(1 + \Gamma_X)$ ,  $\sigma_{p\gamma} \sim 0.7 \times 10^{-28} \text{ cm}^{-2}$  is the cross section for photomeson interaction and  $\tilde{E}_{p-X} =$

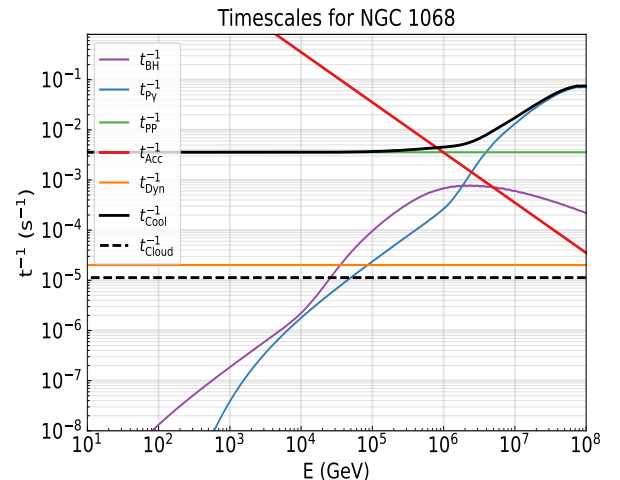


**Figure 1.** Example proton interaction timescales for NGC 1068. Detailed expressions for the timescale calculations are provided in the main text. The adopted parameters are:  $\mathcal{R} = 15$ ,  $\epsilon_B = 0.01$ ,  $\eta_k = 0.1$ , and  $v_0 = 0.03c$ .

$0.5m_p c^2 \cdot 0.3 \text{ GeV}/\epsilon_X$  is the typical proton energy interacted with photons of energy  $\epsilon_X$  (F. Stecker 1968). From Eq (3) and Eq (4), we can write the timescale ratio between  $pp$  collisions and  $p\gamma$  interaction with corona photons as

$$\frac{t_{p\gamma,X}}{t_{pp}} \simeq 72.1 \eta_{k,-1} L_{\text{bol},45} L_{X,43.7}^{-1} \left( \frac{v_0}{0.03c} \right)^{-3} \left( \frac{E_p}{50 \text{ TeV}} \right)^{-1}. \quad (5)$$

The observed neutrino energies from Seyfert galaxies are in the range  $E_\nu \sim 0.3 - 30 \text{ TeV}$  (excluding NGC 7469, from which neutrino energies  $> 100 \text{ TeV}$ ), implying parent proton energies of  $E_p \sim 6 - 600 \text{ TeV}$ , with a typical energy ratio of  $\sim 20$  between parent protons and neutrinos produced. From Eq (5), the corresponding timescale ratio in this proton energy range is  $t_{p\gamma,X}/t_{pp} \sim 6.0 - 600.8$ , suggesting that the  $p\gamma$  interaction with X-ray photons is much less efficient than the  $pp$  collision in producing neutrinos. Similarly, for the  $p\gamma$  process between protons and disk photons, we have

$$\begin{aligned} t_{p\gamma,d}^{-1} &\simeq \frac{\sigma_{p\gamma} L_{\text{bol}}}{4\pi r_0^2 \epsilon_d} \\ &\simeq 0.06 L_{\text{bol},45} \left( \frac{\mathcal{R}}{15} \right)^{-2} R_{s,12.5}^{-2} \left( \frac{\epsilon_d}{30 \text{ eV}} \right)^{-1} \text{ s}^{-1}, \end{aligned} \quad (6)$$

where the disk luminosity is approximated by the bolometric luminosity  $L_{\text{bol}}$  and  $\epsilon_d$  is the characteristic photon energy of the disk (J.-H. Woo & C. M. Urry 2002). We can also evaluate the timescale ratio between  $p\gamma$  interaction with the disk photon and the  $pp$  collisions as

$$\frac{t_{p\gamma,d}}{t_{pp}} \simeq 0.06 \eta_{k,-1} \left( \frac{v_0}{0.03c} \right)^{-3} \left( \frac{\epsilon_d}{30 \text{ eV}} \right)^{-1}, \quad (7)$$

which suggests that this process could dominate over  $pp$  collisions. However, the typical proton energy required for this interaction is  $\tilde{E}_{p-X} = 0.5m_p c^2 \cdot 0.3 \text{ GeV}/\epsilon_d \simeq 5 \text{ PeV}$ . The corresponding neutrino energy is  $\sim 250 \text{ TeV}$ , which is much greater than most of the observed neutrino energies, implying that this process may contribute to the highest end of the neutrino spectrum but is unlikely to account for the entire observed energy range. Therefore,  $pp$  collisions are expected to be the dominant mechanism for neutrino production in this model.

Protons may lose energy through the Bethe-Heitler (BH) process at lower energies, which could suppress neutrino production in the low-energy band. The maximum efficiency of this process occurs during interactions

with disk photons, for which the timescale is

$$\begin{aligned} t_{\text{BH},d}^{-1} &\simeq \frac{\sigma_{\text{BH}} L_{\text{bol}}}{4\pi r_0^2 \epsilon_d} \\ &\simeq 6 \times 10^{-4} L_{\text{bol},45} \left( \frac{\mathcal{R}}{15} \right)^{-2} R_{s,12.5}^{-2} \left( \frac{\epsilon_d}{30 \text{ eV}} \right) \text{ s}^{-1}, \end{aligned} \quad (8)$$

where BH cross section is taken as  $\sigma_{\text{BH}} \sim 0.8 \times 10^{-30} \text{ cm}^{-2}$ . The typical proton energy is  $\tilde{E}_{\text{BH}-X} = 0.5m_p c^2 \cdot 10 \text{ MeV}/\epsilon_d \simeq 156.6 \text{ TeV}$  (M. J. Chodorowski et al. 1992; S. Stepney & P. W. Guilbert 1983). At this proton energy, the corresponding  $p\gamma$  process is dominated by interactions with X-ray photons. We find  $t_{\text{BH},d}/t_{p\gamma,X} \approx 0.11$  and  $t_{\text{BH},d}/t_{pp} \approx 5$ , suggesting that although the BH process dominates over the  $p\gamma$  channel in the low-energy regime, it remains less efficient than  $pp$  collisions. Therefore, the overall suppression of neutrino production due to the BH process should be limited, in contrast to the results in (Y. Inoue et al. 2020; K. Murase et al. 2020), where BH-induced suppression was considered significant because only the  $p\gamma$  channel was taken into account in their scenarios.

We define the total proton cooling timescale as  $t_{\text{cool}}^{-1} = t_{pp}^{-1} + t_{p\gamma}^{-1} + t_{\text{BH}}^{-1}$ , where  $t_{p\gamma}$  and  $t_{\text{BH}}$  include contributions from both disk and X-ray photons. The maximum proton energy,  $E_{p,\text{max}}$ , can then be determined via  $t_{\text{acc}} = \min\{t_{\text{cool}}, t_{\text{cloud}}\}$ . From Eq (3)- Eq (8), we typically find that  $t_{\text{cool}}/t_{\text{cloud}} \ll 1$ , indicating that  $E_{p,\text{max}}$  is generally constrained by radiative cooling rather than the cloud's dynamical lifetime. Assuming the proton radiative cooling is dominated by  $pp$  collisions, we can combine Eq (2) and (3) to write the formula for  $E_{p,\text{max}}$  as

$$\begin{aligned} E_{p,\text{max}} &\simeq 1 \left( \frac{\epsilon_{B,-2}}{\eta_{k,-1}} \right)^{1/2} L_{\text{bol},45}^{-1/2} \\ &\times \left( \frac{\mathcal{R}}{15} \right) R_{s,12.5} \left( \frac{v_0}{0.03c} \right)^{9/2} \text{ PeV}. \end{aligned} \quad (9)$$

The example proton interaction timescales for NGC 1068 are illustrated in Fig.1, and show good agreement with the above analytical expectations. The detailed timescale for the  $p\gamma$  is calculated via

$$t_{p\gamma}^{-1} = \frac{c}{2\gamma_p^2} \int_{\tilde{E}_{\text{th}}}^{\infty} d\tilde{E} \sigma_{p\gamma}(\tilde{E}) \kappa_{p\gamma}(\tilde{E}) \tilde{E} \int_{\tilde{E}/2\gamma_p}^{\infty} dE_\gamma E_\gamma^{-2} \frac{dN_\gamma}{dE_\gamma}, \quad (10)$$

where  $\sigma_{p\gamma}$  and  $\kappa_{p\gamma}$  are the cross-section and inelasticity, respectively (F. Stecker 1968; C. Patrignani et al. 2016),  $\tilde{E}$  is the photon energy in the proton rest frame, and  $\tilde{E}_{\text{th}} \simeq 145 \text{ MeV}$  is the threshold energy. Here,  $\gamma_p = E_p/(m_p c^2)$  is the proton Lorentz factor, and  $dN_\gamma/dE_\gamma$  is the differential number density of the corona/disk photon. The BH process timescale  $t_{\text{BH}}$  is calculated using

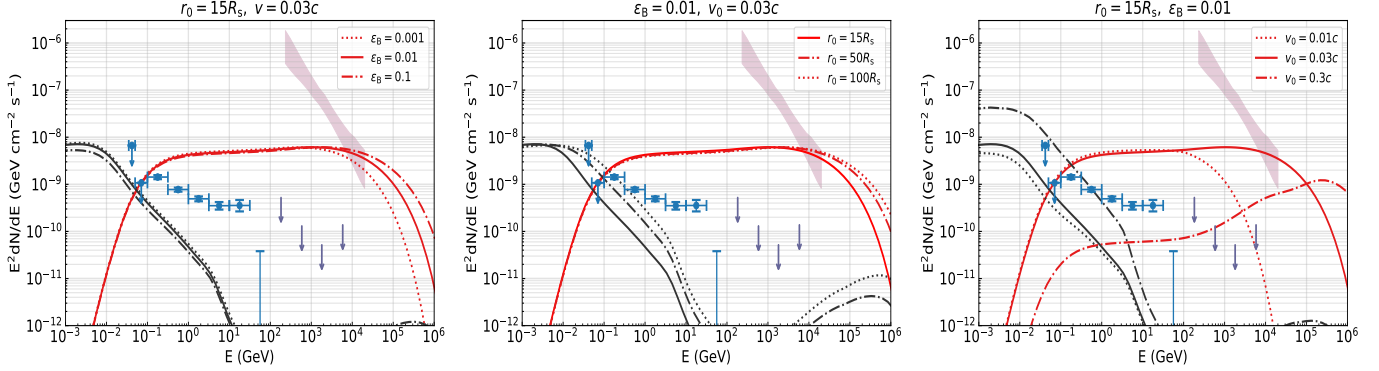


**Figure 2.** The all-flavor neutrino and gamma-ray fluxes for NGC 1068 under various parameter combinations, with the proton spectral index fixed at  $\Gamma_p = 2$  and energy conversion efficiency  $\eta_k = 0.1$ . Red lines (with different linestyles) represent the predicted neutrino fluxes, while black lines denote the corresponding cascade photon fluxes. Blue data points show Fermi-LAT 16-year observations, and purple arrows indicate MAGIC upper limits (V. A. Acciari et al. 2019). The pink shaded region marks the neutrino flux detected by IceCube (R. Abbasi et al. 2025).

the same expression, with  $\sigma_{p\gamma}$  and  $\kappa_{p\gamma}$  replaced by the corresponding quantities  $\sigma_{BH}$  and  $\kappa_{BH}$  (M. J. Chodowski et al. 1992). With the timescales, we can estimate the neutrino flux for NGC 1068 as (K. Murase et al. 2016; X.-Y. Wang & Z.-G. Dai 2009)

$$E_\nu^2 \frac{dN_\nu}{dE_\nu} \simeq \frac{1}{4\pi d_L^2} \frac{3K}{4(1+K)} f_{pp} A_n L_p \stackrel{(\Gamma_p \approx 2)}{\simeq} 1 \times 10^{-8} \eta_{k,-1} L_{bol,45} \text{ GeV cm}^{-2} \text{ s}^{-1}. \quad (11)$$

which is comparable to the observed flux. Here,  $d_L = 14.4$  Mpc is the luminosity distance of NGC 1068 (R. Abbasi et al. 2022), and  $K = 2$  is adopted for the  $pp$ -dominated case (K. Murase et al. 2016). The parameter  $A_n$  denotes the normalization of the proton spectrum; typically,  $A_n \simeq 0.07$  for a proton spectral index of  $\Gamma_p = 2$ . The factor  $f_{pp}$  represents the efficiency of  $pp$  collisions, defined as  $f_{pp} = \min\{1, t_{dyn}/t_{pp}\}$ , where  $t_{dyn} = r_0/v_0$  is the dynamical timescale.

In summary, within our model, the dominant hadronic channel responsible for the observed neutrinos is the  $pp$  collision between accelerated protons and cold protons from the outflow. The  $p\gamma$  process involving disk photons may contribute marginally, but only at the highest neutrino energies. The suppression caused by the BH process is expected to be limited.

### 3. NEUTRINOS FROM SEYFERT GALAXIES

#### 3.1. Individual Sources

In this section, we numerically compute the neutrino and gamma-ray spectra for neutrino-detected Seyfert galaxies. Overall, we take the cloud parameters  $n_c = 5 \times 10^{22} \text{ cm}^{-3}$  and  $r_c = 10^9 \text{ cm}$  to be constant, while treating  $\mathcal{R}$ ,  $\epsilon_B$ ,  $\eta_k$ , and  $v_0$  as free parameters. We assume the accelerated protons follow a single power-law

distribution with an exponential cutoff (R. Blandford & D. Eichler 1987), normalized by the outflow kinetic energy density at  $r_0$ :

$$\int_{1 \text{ GeV}}^{\infty} E_p^{1-\Gamma_p} \exp\left(-\frac{E_p}{E_{p,\max}}\right) dE_p = \frac{L_p}{2\pi r_0^2 v_0}. \quad (12)$$

We calculate neutrino, gamma-ray, and electron (positron) productions using the methods of S. R. Kelner et al. (2006) and S. Kelner & F. Aharonian (2008) for  $pp$  collisions and  $p\gamma$  interactions, respectively. To account for proton energy losses, a suppression factor  $f_c = \min\{1, t_{cool}/t_{dyn}\}$  is applied to the production spectrum to rescale the neutrino yield. The corona and disk radiation fields attenuate the gamma-rays produced alongside neutrinos via  $\gamma\gamma$  pair production. The optical depth due to the corona is estimated as (K. Murase et al. 2020)

$$\tau_{\gamma\gamma,X} \simeq 0.1 \sigma_T \frac{L_X}{4\pi r_0 \epsilon_X} \left( \frac{E_\gamma}{\tilde{E}_{\gamma-X}} \right)^{\Gamma_X-1} \stackrel{(\Gamma_X \approx 2)}{\simeq} 472 L_{X,43.7} \left( \frac{\mathcal{R}}{15} \right)^{-1} R_{s,12.5}^{-1} \left( \frac{E_\gamma}{1 \text{ GeV}} \right), \quad (13)$$

where  $E_\gamma$  is the gamam-ray photon energy,  $\sigma_T$  is the Thomson scattering cross section,  $\tilde{E}_{\gamma-X} \approx m_e^2 c^4 / \epsilon_X$  is the typical gamma-ray photon energy.  $\tau_{\gamma\gamma,X}(1 \text{ GeV}) \gg 1$  indicates that the initial gamma-rays are expected to cascade down to sub-GeV energies, as previously discussed in K. Murase et al. (2020); K. Murase (2022); A. Das et al. (2024). We adopt the method of M. Böttcher et al. (2013) to compute the steady-state electron (positron) spectrum resulting from cascading. Both synchrotron emission and inverse Compton scattering with soft photon fields are considered to derive the final photon spectrum. Detailed description for this method

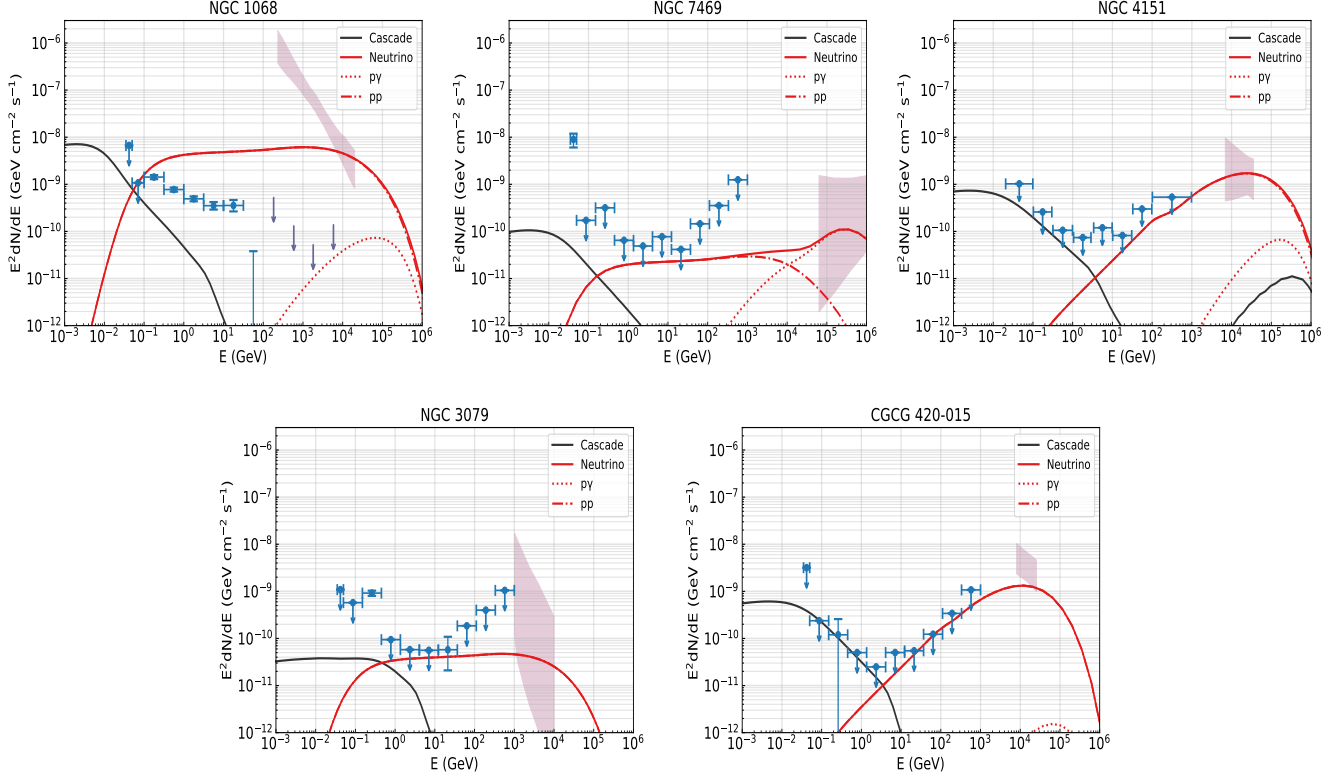


**Figure 3.** The all-flavor neutrino and gamma-ray SEDs for five neutrino-associated sources: NGC 1068, NGC 4151, NGC 3079, CGCG 420-015, and NGC 7469. Blue points represent the 16-year Fermi-LAT gamma-ray data. The shaded regions indicate the neutrino fluxes detected by IceCube, with data sourced from R. Abbasi et al. (2025) for NGC 7469, NGC 4151, and CGCG 420-015, and from A. Neronov et al. (2024) for NGC 3079.

is presented in Appendix A. For numerical calculations, the optical depth for gamma rays is evaluated as (Y. Inoue et al. 2019)

$$\tau_{\gamma\gamma} = \int_{-1}^1 d\mu \int_{\epsilon_{\text{th}}}^{\infty} d\epsilon \frac{1-\mu}{2} \frac{dn_{\{\text{X,d}\}}}{d\epsilon} \sigma_{\gamma\gamma}(E_{\gamma}, \epsilon, \theta) r_0, \quad (14)$$

where  $\mu = \cos \theta$ ,  $\epsilon_{\text{th}} = \frac{2m_e^2 c^4}{E_{\gamma}(1-\mu)}$  is the pair production threshold energy, and  $dn_{\{\text{X,d}\}}/d\epsilon$  is the differential number density of soft photons from corona or disk. The pair production cross section is given by (G. Breit & J. A. Wheeler 1934; W. Heitler 1954):

$$\sigma_{\gamma\gamma}(E_{\gamma}, \epsilon, \theta) = \frac{3\sigma_T}{16} (1 - \beta^2) \times \left[ 2\beta(\beta^2 - 2) + (3 - \beta^4) \ln \left( \frac{1 + \beta}{1 - \beta} \right) \right], \quad (15)$$

where

$$\beta = \sqrt{1 - \frac{2m_e^2 c^4}{E_{\gamma} \epsilon (1 - \mu)}}. \quad (16)$$

IceCube has identified several Seyfert galaxies as potential neutrino sources, including NGC 1068,

NGC 7469, NGC 4151, NGC 3079, and CGCG 420-015. The SED of soft radiation fields for these five nuclei is shown in Appendix B. As noted in previous studies, gamma-ray emissions in the Fermi-LAT energy band provide strong constraints on electromagnetic cascades, thereby limiting the range of viable model parameters (A. Das et al. 2024; K. Murase et al. 2024). To investigate these constraints, we analyze 16 years of Fermi-LAT data to derive the gamma-ray fluxes and 95% C.L. upper limits for these five sources. The detailed processing is in Appendix C. We then apply our theoretical model and compare the numerical predictions with the observed fluxes.

Fig. 2 presents the SEDs from our model for NGC 1068 under various parameter configurations. The fiducial model adopts  $\mathcal{R} = 15$ ,  $\epsilon_B = 0.01$ ,  $\eta_k = 0.1$ ,  $v_0 = 0.03c$ , and a proton spectral index of  $\Gamma_p = 2$ . To investigate the impact of physical parameters, we vary  $\mathcal{R}$ ,  $\epsilon_B$  and  $v_0$  individually while keeping the other parameters fixed. From Fig. 2, we observe that the magnetic parameter  $\epsilon_B$  affects the maximum energy of neutrinos, but has a negligible impact on the overall flux amplitude. This is because  $\epsilon_B$  only weakly influences the maximum proton energy, following the relation  $E_{p,\text{max}} \propto \epsilon_B^{1/2}$ , from

**Table 1.** Model parameters corresponding to the numerical results shown in Fig. 3. The SMBH mass ( $M_\bullet$ ) and intrinsic X-ray luminosity  $L_X$  (in the 2–10 keV band) are adopted from the literature; references are listed in the notes. The last five columns correspond to the model’s free parameters.

Source Name	$M_\bullet (M_\odot)$	$L_X (\text{erg s}^{-1})$	$v_0 (c)$	$\mathcal{R}$	$\epsilon_B$	$\eta_k$	$\Gamma_p$
NGC 1068 <sup>a</sup>	$1.0 \times 10^7$	$7.0 \times 10^{43}$	0.030	15	0.01	0.1	2.0
NGC 7469 <sup>e</sup>	$1.0 \times 10^7$	$2.3 \times 10^{43}$	0.300	15	0.01	0.4	2.0
NGC 4151 <sup>b</sup>	$1.0 \times 10^7$	$2.6 \times 10^{42}$	0.030	14	0.01	0.4	1.2
NGC 3079 <sup>c</sup>	$2.0 \times 10^6$	$1.0 \times 10^{42}$	0.015	40	0.01	0.1	2.0
CGCG 420-015 <sup>d</sup>	$2.0 \times 10^8$	$7.0 \times 10^{43}$	0.020	10	0.01	0.1	1.2

<sup>a</sup> J.-H. Woo & C. M. Urry (2002); A. Marinucci et al. (2015)

<sup>b</sup> M. C. Bentz et al. (2022); M. J. Koss et al. (2022)

<sup>c</sup> P. T. Kondratko et al. (2005); N. Iyomoto et al. (2001)

<sup>d</sup> M. Koss et al. (2017); A. Tanimoto et al. (2018)

<sup>e</sup> B. Peterson et al. (2014); C. Ricci et al. (2021)

Eq (9). The corresponding neutrino flux amplitude is thus affected by the normalization factor, which scales as  $\propto \ln^{-1}(E_{p,\text{max}}/1 \text{ GeV})$  for a proton spectral index of  $\Gamma_p = 2$ . When  $\epsilon_B$  increases by one order of magnitude, the normalization factor only decreases by  $\sim 0.5$ . Since the change in normalization is minimal, the resulting flux remains largely unchanged. Similar rules can be found in the case of parameter  $\mathcal{R}$ , the maximum neutrino energy scales with  $r_0$ , with relation  $E_{p,\text{max}} \propto r_0$  from Eq (9), while the overall flux amplitude remains nearly unchanged. The independence of the neutrino flux from  $r_0$  can also be understood as follows: the final neutrino spectrum is normalized by the kinetic luminosity  $L_{\text{kin}}$ , which is independent of  $r_0$ . The parameter  $v_0$  has the most pronounced impact on the resulting neutrino flux, primarily because it strongly affects the  $pp$  interaction efficiency, as indicated by Eq (3), where  $t_{pp} \propto v_0^3$ . At high velocities (e.g.,  $v_0 = 0.3c$ ), the  $p\gamma$  interactions with disk photons begin to dominate neutrino production at the highest energies, resulting in a rising feature in the spectrum, as shown in the  $v_0 = 0.3c$  case in Fig. 2.

We then extend our analysis to additional neutrino-associated Seyfert galaxies. The numerical results, together with the observed fluxes, are shown in Fig. 3, and the corresponding model parameters for each source are summarized in Table 1. We find that both NGC 1068 and NGC 3079 can be well explained by the model with a proton spectral index of  $\Gamma_p = 2$ . In contrast, for NGC 4151 and CGCG 420-015, a harder proton index is required to avoid cascade emission exceeding the 95% C.L. upper limits. NGC 7469 is the most exceptional case, as two neutrinos with energy  $> 100 \text{ TeV}$  have been detected from this source, significantly more energetic than neutrinos from the others. However, our model can naturally account for the neutrino flux in this high-

energy band, as  $p\gamma$  interactions with disk photons can contribute at these energies. This requires a fast outflow velocity in the source, specifically  $v_0 = 0.3c$ . In most cases, the required outflow velocities range from  $0.01c$  to  $0.03c$ , and the kinetic-to-bolometric luminosity ratio  $\eta_k$  lies between 0.1 and 0.4.

### 3.2. Diffuse Neutrinos and Gamma Rays

The cumulative contribution of Seyfert galaxies to the diffuse neutrino background has also been explored in several works (P. Padovani et al. 2024a; K. Murase et al. 2020; D. F. Fiorillo et al. 2025). While such AGNs are promising candidates, the overall contribution remains

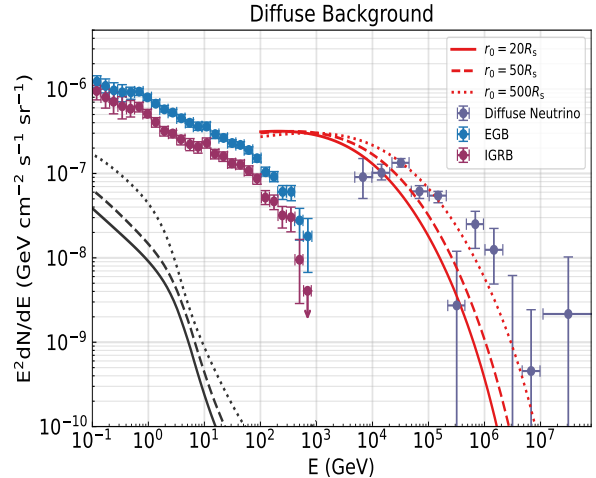


**Figure 4.** Diffuse neutrino and gamma-ray contributions from a population of Seyfert galaxies, assuming the Schwarzschild radius of  $R_s = 10^{12.5} \text{ cm}$ , which corresponds to an SMBH with mass  $M_{\text{BH}} = 10^7 M_\odot$ . The extragalactic gamma-ray background (EGB) and isotropic gamma-ray background (IGRB) data are taken from M. Ackermann et al. (2015), while the diffuse neutrino background data are adopted from R. Naab et al. (2023).

uncertain due to the diversity of source environments and model parameters. Here, we also extend our study to the diffuse neutrino and gamma-ray fluxes originating from a population of Seyfert galaxies. The diffuse neutrino flux can be calculated as (K. Murase et al. 2014; R.-Y. Liu et al. 2018; D. F. Fiorillo et al. 2025)

$$E_\nu^2 \Phi_\nu(E_\nu) = \frac{c}{4\pi H_0} \int_0^{z_{\max}} \frac{dz}{\sqrt{(1+z)^3 \Omega_M + \Omega_\Lambda}} \times \int d \log L_X \frac{d\Psi}{d \log L_X} \frac{L_\nu[(1+z)E_\nu]}{(1+z)^2}, \quad (17)$$

where  $H_0 = 67.8 \text{ km s}^{-1} \text{ Mpc}^{-1}$  is the Hubble constant, and the cosmological parameters are  $\Omega_M = 0.308$  and  $\Omega_\Lambda = 0.692$  (P. A. Ade et al. 2016). Here,  $L_\nu$  denotes the neutrino luminosity in the source frame, and  $d\Psi/d \log L_X$  represents the comoving number density of AGNs per logarithmic X-ray luminosity interval, as defined in Y. Ueda et al. (2014). The diffuse gamma-ray flux can be computed using the same formalism, by replacing  $L_\nu$  with the gamma-ray luminosity  $L_\gamma$ . For the model parameters, we adopt  $\epsilon_B = 0.01$ ,  $\eta_k = 0.1$ , and  $v_0 = 0.03c$ . The resulting diffuse neutrino fluxes for different values of  $r_0$  are shown in Fig. 4. We find that the diffuse neutrino emission from Seyfert galaxies can account for the observed neutrino background in the energy range of  $10^4$ – $10^5$  GeV. In contrast, the associated gamma-ray contribution from cascade emissions is relatively minor, contributing only modestly in the 0.1–10 GeV band.

As the cloud location parameter  $r_0$  increases, the diffuse neutrino flux extends to higher energies. However, when  $r_0 > 20R_{s,12.5}$ , the predicted flux may exceed the observed diffuse neutrino flux around  $10^4$  GeV. Therefore, we constrain the typical cloud location to  $r_0 < 20R_{s,12.5}$  for the Seyfert galaxy population. Under this constraint, the corresponding diffuse gamma-ray flux contribution remains below 4%.

#### 4. SUMMARY

Seyfert galaxies are among the most promising candidates for high-energy neutrino sources. AGNs in these galaxies can drive outflows with mildly relativistic ve-

locities that collide with dense clouds surrounding the SMBH. These outflow–cloud interactions provide natural sites for proton acceleration, leading to the production of high-energy neutrinos.

In this work, we extend the outflow–cloud interaction model to a broader population of Seyfert galaxies. We perform a detailed analysis of the hadronic processes involved and identify the dominant neutrino production channel as  $pp$  collisions between accelerated protons and cold protons in the outflow. The  $p\gamma$  process, involving disk photons, contributes only marginally, and only at the highest neutrino energies. Suppression due to the BH process is found to be limited. We also investigate the dependence of the model on key parameters, using NGC 1068 as a representative case.

We then apply the model to five individual Seyfert galaxies and find that their neutrino and gamma-ray emissions can be reasonably explained. However, a harder proton spectral index is required to match the observations of NGC 4151 and CGCG 420–015. Finally, we estimate the diffuse neutrino and gamma-ray fluxes from the entire Seyfert galaxy population. Our results show that Seyfert galaxies can account for the observed neutrino background in the energy range of  $10^4$ – $10^5$  GeV. To avoid exceeding the observed diffuse flux, we constrain the typical cloud location to  $r_0 < 20R_{s,12.5}$ . Under this condition, the corresponding diffuse gamma-ray flux contribution remains below 4%.

Future observations by next-generation neutrino detectors such as IceCube-Gen2 (M. G. Aartsen et al. 2021) and KM3NeT (A. Margiotta et al. 2014), as well as upcoming MeV to sub-GeV gamma-ray missions like e-ASTROGAM (A. De Angelis et al. 2018) and AMEGO (H. Fleischhack 2021), will offer valuable opportunities to further test and constrain the outflow–cloud interaction scenario in Seyfert galaxies.

#### ACKNOWLEDGMENTS

We acknowledge support from the National Natural Science Foundation of China under grant No.12003007 and the Fundamental Research Funds for the Central Universities (No. 2020kfyXJJS039).

#### APPENDIX

##### A. CASCADE PROCESS

High-energy gamma rays produced through hadronic processes are attenuated by soft photons from the accretion disk or X-ray corona, resulting in the production of electron–positron pairs. These high-energy pairs subsequently emit gamma rays via synchrotron radiation and inverse Compton scattering, initiating an electromagnetic cascade

that continues until a steady state is reached. We follow the method proposed by [M. Böttcher et al. \(2013\)](#) to calculate the emission from stable electrons (positrons) produced in the electromagnetic cascade. The steady state electron (positron) distribution,  $N_e(\gamma)$ , satisfies the isotropic Fokker–Planck equation:

$$\frac{\partial}{\partial \gamma} (\dot{\gamma} N_e[\gamma]) = Q_e(\gamma) + \dot{N}_e^{\gamma\gamma}(\gamma) + \dot{N}_e^{\text{esc}}, \quad (\text{A1})$$

where  $\gamma$  is the electron (positron) Lorentz factor. The term  $Q_e(\gamma)$  represents the injection rate of electrons (positrons) from both photomeson and Bethe–Heitler (BH) processes. The escape term is energy-independent and given by  $\dot{N}_e^{\text{esc}} = -N_e(\gamma)/t_{\text{esc}}$ , where the escape timescale is  $t_{\text{esc}} = r_0/c$ . The total energy loss rate,  $\dot{\gamma} = \dot{\gamma}_{\text{syn}} + \dot{\gamma}_{\text{Com}}$ , includes contributions from both synchrotron radiation and inverse Compton scattering with soft photon fields (from the disk and corona). The term  $\dot{N}_e^{\gamma\gamma}(\gamma)$  denotes the injection rate of electrons (positrons) due to  $\gamma\gamma$  absorption, which is given by

$$\dot{N}_e^{\gamma\gamma}(\gamma) = f_{\text{abs}}(\epsilon_1) \left( \dot{N}_{\epsilon_1}^0 + \dot{N}_{\epsilon_1}^{\text{syn}} + \dot{N}_{\epsilon_1}^{\text{Com}} \right) + f_{\text{abs}}(\epsilon_2) \left( \dot{N}_{\epsilon_2}^0 + \dot{N}_{\epsilon_2}^{\text{syn}} + \dot{N}_{\epsilon_2}^{\text{Com}} \right), \quad (\text{A2})$$

where the energies of the absorbed high-energy photons are  $\epsilon_1 = \gamma/f_\gamma$  and  $\epsilon_2 = \gamma/(1-f_\gamma)$ , with  $f_\gamma = 0.9$ . The absorption factor is defined as  $f_{\text{abs}}(\epsilon) = 1 - \frac{1-e^{-\tau(\epsilon)}}{\tau(\epsilon)}$ , where the optical depth  $\tau(\epsilon)$  is computed from Eq. (13). The steady-state electron distribution  $N_e(\gamma)$  is given as the implicit solution to Eq. (A1):

$$N_e(\gamma) = \frac{1}{\dot{\gamma}} \int_\gamma^\infty d\tilde{\gamma} \left\{ Q_e(\tilde{\gamma}) + \dot{N}_e^{\gamma\gamma}(\tilde{\gamma}) - \frac{N_e(\tilde{\gamma})}{t_{\text{esc}}} \right\}. \quad (\text{A3})$$

Equation (A3) can be solved iteratively, starting from the highest values of  $\gamma$ . Once the steady-state electron (positron) distribution is obtained, the resulting cascade emission can be calculated from synchrotron radiation and inverse Compton scattering.

## B. SOFT PHOTON FIELDS

We can uniformly model the spectral energy distribution of soft radiation fields for all AGNs using only the SMBH mass  $M_\bullet$  and the observed X-ray luminosity  $L_X$  in the 2–10 keV band, following the method proposed by [K. Murase et al. \(2020\)](#). The soft radiation in the corona region consists of two components: optical/UV emission from the accretion disk and X-ray emission from the corona. For the disk emission, the averaged SEDs are expressed as a function of the Eddington ratio,  $\lambda_{\text{Edd}} = L_{\text{bol}}/L_{\text{Edd}}$  (see Figure 7 in [L. C. Ho 2008](#)), where the Eddington luminosity is  $L_{\text{Edd}} \approx 1.3 \times 10^{45} M_{\bullet,7} \text{ erg s}^{-1}$ , and the bolometric luminosity can be obtained through ([P. F. Hopkins et al. 2007](#)):

$$\frac{L_{\text{bol}}}{L_X} = 10.83 \left( \frac{L_{\text{bol}}}{10^{10} L_\odot} \right)^{0.28} + 6.08 \left( \frac{L_{\text{bol}}}{10^{10} L_\odot} \right)^{-0.02}, \quad (\text{B4})$$

where  $L_\odot$  is the solar luminosity. The disk emission is expected to cut off at a certain energy, above which the X-ray component becomes dominant. The cutoff energy, denoted as  $\epsilon_d$  (also used as the characteristic disk photon energy in Sec. 2), is determined by the effective temperature at the innermost stable circular orbit (ISCO):  $T_d \simeq 0.49 \left( \frac{GM_\bullet \dot{M}_\bullet}{72\pi\sigma_{\text{SB}} R_s^3} \right)^{1/4}$ , where  $\sigma_{\text{SB}}$  is the Stefan–Boltzmann constant, and the SMBH accretion rate is  $\dot{M}_\bullet \simeq L_{\text{bol}}/(\eta_{\text{rad}} c^2)$  with a radiative efficiency  $\eta_{\text{rad}} = 0.1$  ([S. Kato et al. 2008](#)). The corresponding disk cutoff energy is then  $\epsilon_d \simeq 3k_B T_d$ . For the X-ray component, the SED can be modeled as a power law with an exponential cutoff:

$$\frac{dn_X}{d\epsilon_X} \propto \epsilon_X^{-\Gamma_X} \exp\left(-\frac{\epsilon_X}{\epsilon_{X,\text{cut}}}\right), \quad (\text{B5})$$

which is normalized by the observed  $L_X$ . The photon index can be estimated as ([B. Trakhtenbrot et al. 2017b](#))

$$\Gamma_X \approx 0.167 \log(\lambda_{\text{Edd}}) + 2, \quad (\text{B6})$$

and the cutoff energy is given by ([C. Ricci et al. 2018](#))

$$\epsilon_{X,\text{cut}} \approx -74 \log(\lambda_{\text{Edd}}) + 1500 \text{ keV}. \quad (\text{B7})$$

Based on these relations, the combined disk–corona SED of Seyfert nuclei can be constructed once the black hole mass  $M_\bullet$  and X-ray luminosity  $L_X$  are known. For NGC 1068, where clear observations give  $L_{\text{bol}} \simeq 1 \times 10^{45} \text{ erg s}^{-1}$  and  $\epsilon_d \simeq 32 \text{ eV}$ , we adopt these observed values directly. For the remaining four sources, the disk–corona SEDs are derived using the relations described above. The resulting soft-photon SEDs for the five neutrino-associated Seyfert galaxies analyzed in this work are shown in Fig 5.

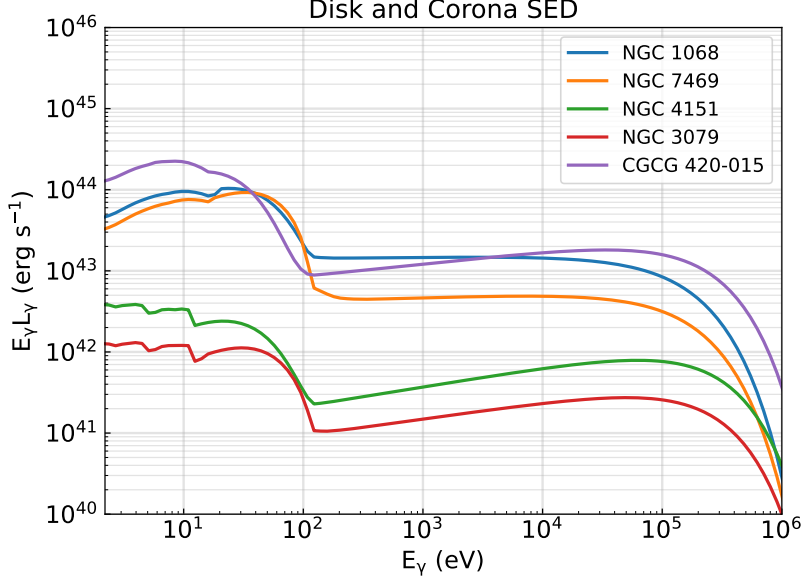


**Figure 5.** Combined disk and corona SEDs for the five neutrino-associated Seyfert nuclei analyzed in this work.

### C. DATA PROCESSING

In this work, we analyze the gamma-ray emission from NGC 1068, NGC 4151, NGC 3079, CGCG 420-015, and NGC 7469, using  $\sim 16.4$  years of Fermi-LAT observations collected between 2008 August 5 and 2025 January 1. The analysis covers the energy range from 30 MeV to 1 TeV. Only data within a  $10^\circ$  region of interest (ROI) centered on the position of these sources are considered. All data are retrieved from the Fermi LAT public data archive<sup>3</sup> and are processed using the Fermipy package (M. Wood et al. 2017). We use the standard data filters: DATA\_QUAL > 0 and LAT\_CONFIG == 1. The photons are selected corresponding to the P8R3\_SOURCE\_V3 instrument response. The Galactic diffuse background and the point-source emission are modeled using the standard component (gll\_iem\_v07.fits) and the 4FGL-DR3 catalog (gll\_psc\_v28.fits; S. Abdollahi et al. (2022)), respectively. To account for photon leakage from sources outside the ROI due to the detector’s point-spread function (PSF), all 4FGL sources within a  $15^\circ$  radius are included in the model. The energy dispersion correction (edisp\_bins = -1) is applied to all sources except for the isotropic component.

Based on the energy dependence of the LAT instrument response, we divide the analysis into two energy regimes: 30-50 MeV and 50 MeV-1 TeV. In the low energy range, the maximum zenith angle is set to  $80^\circ$ , the extragalactic emission, along with the residual instrumental background, is modeled using iso\_P8R3\_SOURCE\_V3\_v1.txt. For the 50 MeV-1 TeV range, to optimize analysis sensitivity, we perform a joint likelihood analysis across four PSF classes (iso\_P8R3\_SOURCE\_V3\_PSFi\_v1.txt, where  $i$  ranges from 0 to 3), adopting a maximum zenith angle of  $90^\circ$ . The data are binned using two energy bins per decade.

Before calculating the spectral energy distributions, we perform an initial model optimization. New sources with test statistics (TS) greater than 25 are identified using the Fermipy function find\_source. The sources are modeled with a power-law spectrum. The spectral parameters (index and normalization) of both the source and the Galactic diffuse component, as well as the normalization of the isotropic component, are left free to vary. In addition, the

<sup>3</sup> <https://fermi.gsfc.nasa.gov/cgi-bin/ssc/LAT/LATDataQuery.cgi>

normalization parameters of all 4FGL sources with  $TS \geq 25$  located within  $5^\circ$  of the ROI center, and of all sources with  $TS \geq 500$  located within  $7^\circ$  are free as well. The SEDs are computed for each source using the Fermipy SED analysis, in which the flux normalization is fit independently in each energy bin, assuming a power-law spectrum with a fixed photon index of 2. Upper limits are reported at the 95% confidence level.

## REFERENCES

- Aartsen, M. G., Abbasi, R., Ackermann, M., et al. 2021, *Journal of Physics G: Nuclear and Particle Physics*, 48, 060501
- Abbasi, R., Ackermann, M., Adams, J., et al. 2022, *Science*, 378, 538
- Abbasi, R., Ackermann, M., Adams, J., et al. 2025, arXiv preprint arXiv:2510.13403
- Abdollahi, S., Acero, F., Baldini, L., et al. 2022, *The Astrophysical Journal Supplement Series*, 260, 53
- Acciari, V. A., Ansoldi, S., Antonelli, L., et al. 2019, *The Astrophysical Journal*, 883, 135
- Ackermann, M., Ajello, M., Albert, A., et al. 2015, *The Astrophysical Journal*, 799, 86
- Ade, P. A., Aghanim, N., Arnaud, M., et al. 2016, *Astronomy & Astrophysics*, 594, A13
- Anchordoqui, L. A., Krizmanic, J. F., & Stecker, F. W. 2021, arXiv preprint arXiv:2102.12409
- Bell, A. 2013, *Astroparticle Physics*, 43, 56
- Bentz, M. C., Williams, P. R., & Treu, T. 2022, *The Astrophysical Journal*, 934, 168
- Blandford, R., & Eichler, D. 1987, *Physics Reports*, 154, 1
- Böttcher, M., Reimer, A., Sweeney, K., & Prakash, A. 2013, *The Astrophysical Journal*, 768, 54
- Breit, G., & Wheeler, J. A. 1934, *Physical Review*, 46, 1087
- Chodorowski, M. J., Zdziarski, A. A., & Sikora, M. 1992, *Astrophysical Journal, Part 1 (ISSN 0004-637X)*, vol. 400, no. 1, p. 181-185., 400, 181
- Collaboration\*, I. 2013, *Science*, 342, 1242856
- Collaboration, I., MAGIC, AGILE, et al. 2018, *Science*, 361, eaat1378
- Czerny, B., & Hryniewicz, K. 2011, *Astronomy & Astrophysics*, 525, L8
- Das, A., Zhang, B. T., & Murase, K. 2024, *The Astrophysical Journal*, 972, 44
- De Angelis, A., Tatischeff, V., Grenier, I. A., et al. 2018, *Journal of High Energy Astrophysics*, 19, 1
- Drury, L. O. 1983, *Reports on Progress in Physics*, 46, 973
- Eichmann, B., Oikonomou, F., Salvatore, S., Dettmar, R.-J., & Tjus, J. B. 2022, *The Astrophysical Journal*, 939, 43
- Fang, K., Rodriguez, E. L., Halzen, F., & Gallagher, J. S. 2023, *The Astrophysical Journal*, 956, 8
- Fiorillo, D. F., Comisso, L., Peretti, E., Petropoulou, M., & Sironi, L. 2025, arXiv preprint arXiv:2504.06336
- Fiorillo, D. F., Petropoulou, M., Comisso, L., Peretti, E., & Sironi, L. 2024, *The Astrophysical Journal Letters*, 961, L14
- Fleischhack, H. 2021, arXiv preprint arXiv:2108.02860
- Gámez Rosas, V., Isbell, J. W., Jaffe, W., et al. 2022, *Nature*, 602, 403
- García-Burillo, S., Combes, F., Almeida, C. R., et al. 2016, *The Astrophysical Journal Letters*, 823, L12
- Harrison, C., Costa, T., Tadhunter, C., et al. 2018, *Nature Astronomy*, 2, 198
- Heitler, W. 1954, *The Quantum Theory of Radiation*, 3rd edn, Clarendon, Oxford
- Ho, L. C. 2008, *Annu. Rev. Astron. Astrophys.*, 46, 475
- Hopkins, P. F., Richards, G. T., & Hernquist, L. 2007, *The Astrophysical Journal*, 654, 731
- Huang, Y.-H., Wang, K., & Ma, Z.-P. 2024, arXiv preprint arXiv:2406.14001
- Inoue, S., Cerruti, M., Murase, K., & Liu, R.-Y. 2022, arXiv preprint arXiv:2207.02097
- Inoue, Y., Khangulyan, D., & Doi, A. 2020, *The Astrophysical Journal Letters*, 891, L33
- Inoue, Y., Khangulyan, D., Inoue, S., & Doi, A. 2019, *The Astrophysical Journal*, 880, 40
- Iyomoto, N., Fukazawa, Y., Nakai, N., & Ishihara, Y. 2001, *The Astrophysical Journal*, 561, L69
- Kato, S., Fukue, J., & Mineshige, S. 2008, *Black-Hole Accretion Disks—Towards a New Paradigm*
- Kelner, S., & Aharonian, F. 2008, *Physical Review D*, 78, 034013
- Kelner, S. R., Aharonian, F. A., & Bugayov, V. V. 2006, *Physical Review D*, 74, 034018
- Kheirandish, A., Murase, K., & Kimura, S. S. 2021, *The Astrophysical Journal*, 922, 45
- King, A., & Pounds, K. 2015, *Annual Review of Astronomy and Astrophysics*, 53, 115
- Klein, R. I., McKee, C. F., & Colella, P. 1994, *Astrophysical Journal, Part 1 (ISSN 0004-637X)*, vol. 420, no. 1, p. 213-236, 420, 213
- Kondratko, P. T., Greenhill, L. J., & Moran, J. M. 2005, *The Astrophysical Journal*, 618, 618

- Koss, M., Trakhtenbrot, B., Ricci, C., et al. 2017, *The Astrophysical Journal*, 850, 74
- Koss, M. J., Trakhtenbrot, B., Ricci, C., et al. 2022, *The Astrophysical Journal Supplement Series*, 261, 1
- Laha, S., Reynolds, C. S., Reeves, J., et al. 2021, *Nature Astronomy*, 5, 13
- Lamastra, A., Fiore, F., Guetta, D., et al. 2016, *Astronomy & Astrophysics*, 596, A68
- Lemoine, M., & Rieger, F. 2025, *Astronomy & Astrophysics*, 697, A124
- Liu, R.-Y., Murase, K., Inoue, S., Ge, C., & Wang, X.-Y. 2018, *The Astrophysical Journal*, 858, 9
- Ma, Z.-P., & Wang, K. 2024, *The Astrophysical Journal*, 970, 127
- Malkov, M., & Drury, L. O. 2001, *Reports on Progress in Physics*, 64, 429
- Margiotta, A., Collaboration, K., et al. 2014, *Nuclear Instruments and Methods in Physics Research Section A: Accelerators, Spectrometers, Detectors and Associated Equipment*, 766, 83
- Marinucci, A., Bianchi, S., Matt, G., et al. 2015, *Monthly Notices of the Royal Astronomical Society: Letters*, 456, L94
- Matt, G., Guainazzi, M., Frontera, F., et al. 1997, arXiv preprint astro-ph/9707065
- Mbarek, R., Philippov, A., Chernoglazov, A., Levinson, A., & Mushotzky, R. 2024, *Physical Review D*, 109, L101306
- McKee, C. F., & Cowie, L. L. 1975, *Astrophysical Journal*, vol. 195, Feb. 1, 1975, pt. 1, p. 715-725., 195, 715
- Mizumoto, M., Izumi, T., & Kohno, K. 2019, *The Astrophysical Journal*, 871, 156
- Mou, G., & Wang, W. 2021, *Monthly Notices of the Royal Astronomical Society*, 507, 1684
- Murase, K. 2022, *The Astrophysical Journal Letters*, 941, L17
- Murase, K., Guetta, D., & Ahlers, M. 2016, *Physical Review Letters*, 116, 071101
- Murase, K., Inoue, Y., & Dermer, C. D. 2014, *Physical Review D*, 90, 023007
- Murase, K., Ioka, K., Nagataki, S., & Nakamura, T. 2008, *Physical Review D—Particles, Fields, Gravitation, and Cosmology*, 78, 023005
- Murase, K., Karwin, C. M., Kimura, S. S., Ajello, M., & Buson, S. 2024, *The Astrophysical Journal Letters*, 961, L34
- Murase, K., Kimura, S. S., & Meszaros, P. 2020, *Physical review letters*, 125, 011101
- Naab, R., Ganster, E., & Zhang, Z. 2023, arXiv preprint arXiv:2308.00191
- Naddaf, M.-H., & Czerny, B. 2024, *Universe*, 10, 29, doi: [10.3390/universe10010029](https://doi.org/10.3390/universe10010029)
- Neronov, A., Savchenko, D., & Semikoz, D. 2024, *Physical Review Letters*, 132, 101002
- Padovani, P., Gilli, R., Resconi, E., Bellenghi, C., & Henningsen, F. 2024a, *Astronomy & Astrophysics*, 684, L21
- Padovani, P., Resconi, E., Ajello, M., et al. 2024b, *Nature Astronomy*, 8, 1077
- Particle, D. 2004, *Phys. Lett. B*, 592, 1
- Passy, J.-C., Mac Low, M.-M., & De Marco, O. 2012, *The Astrophysical Journal Letters*, 759, L30
- Patrignani, C., Particle Data Group, Agashe, K., et al. 2016, *Chinese Physics C*, 40, 100001, doi: [10.1088/1674-1137/40/10/100001](https://doi.org/10.1088/1674-1137/40/10/100001)
- Peretti, E., Peron, G., Tombesi, F., et al. 2023, arXiv preprint arXiv:2303.03298
- Peterson, B., Grier, C., Horne, K., et al. 2014, *The Astrophysical Journal*, 795, 149
- Ricci, C., Ho, L. C., Fabian, A. C., et al. 2018, *Monthly Notices of the Royal Astronomical Society*, 480, 1819
- Ricci, C., Privon, G., Pfeifle, R., et al. 2021, *Monthly Notices of the Royal Astronomical Society*, 506, 5935
- Rossi, E. M., Stone, N. C., Law-Smith, J. A., et al. 2021, *Space Science Reviews*, 217, 1
- Shakura, N. I., & Sunyaev, R. A. 1973, *Astronomy and Astrophysics*, Vol. 24, p. 337-355, 24, 337
- Sommani, G., Franckowiak, A., Lincetto, M., & Dettmar, R.-J. 2025, *The Astrophysical Journal*, 981, 103
- Stecker, F. 1968, *Physical Review Letters*, 21, 1016
- Stepney, S., & Guilbert, P. W. 1983, *Monthly Notices of the Royal Astronomical Society*, 204, 1269
- Tanimoto, A., Ueda, Y., Kawamuro, T., et al. 2018, *The Astrophysical Journal*, 853, 146
- Trakhtenbrot, B., Ricci, C., Koss, M. J., et al. 2017a, arXiv preprint arXiv:1705.01550
- Trakhtenbrot, B., Ricci, C., Koss, M. J., et al. 2017b, *Monthly Notices of the Royal Astronomical Society*, 470, 800
- Ueda, Y., Akiyama, M., Hasinger, G., Miyaji, T., & Watson, M. G. 2014, *The Astrophysical Journal*, 786, 104
- Veilleux, S., Cecil, G., & Bland-Hawthorn, J. 2005, *Annu. Rev. Astron. Astrophys.*, 43, 769
- Wang, J.-M., Du, P., Baldwin, J. A., et al. 2012, *The Astrophysical Journal*, 746, 137
- Wang, X.-Y., & Dai, Z.-G. 2009, *The Astrophysical Journal*, 691, L67
- Woo, J.-H., & Urry, C. M. 2002, *The Astrophysical Journal*, 579, 530

- Wood, M., Caputo, R., Charles, E., et al. 2017, in International Cosmic Ray Conference, Vol. 301, 35th International Cosmic Ray Conference (ICRC2017), 824, doi: [10.22323/1.301.0824](https://doi.org/10.22323/1.301.0824)
- Wu, H., Wang, W., & Wang, K. 2024, *PhRvD*, 110, 043029, doi: [10.1103/PhysRevD.110.043029](https://doi.org/10.1103/PhysRevD.110.043029)
- Wu, H.-J., Mou, G., Wang, K., Wang, W., & Li, Z. 2022, *Monthly Notices of the Royal Astronomical Society*, 514, 4406
- Zhou, Z.-H., & Wang, K. 2023, *The Astrophysical Journal Letters*, 958, L12
- Zhou, Z.-H., Zhu, J.-P., & Wang, K. 2023, *The Astrophysical Journal*, 951, 74
- Zhu, J.-P., Wang, K., & Zhang, B. 2021, *ApJL*, 917, L28